Room temperature ppt-level NO_2 gas sensor based on SnO_x/SnS nanostructures with rich oxygen vacancies

Tang, Hongyu; Gao, Chenshan; Yang, Huiru; Sacco, Leandro; Sokolovskij, Robert; Ye, Huaiyu; Vollebregt, Sten; Fan, Xuejun; Zhang, Guoqi ; More Authors

DOI
10.1088/2053-1583/ac13c1

Publication date
2021

Document Version
Final published version

Published in
2D Materials

2D Materials

PAPER • OPEN ACCESS

Room temperature ppt-level NO_2 gas sensor based on SnO_x/SnS nanostructures with rich oxygen vacancies

To cite this article: Hongyu Tang *et al* 2021 *2D Mater.* **8** 045006

2D Materials

CrossMark

OPEN ACCESS

RECEIVED
6 July 2020

REVISED
26 June 2021

ACCEPTED FOR PUBLICATION
12 July 2021

PUBLISHED
28 July 2021

PAPER

Room temperature ppt-level NO_2 gas sensor based on SnO_x/SnS nanostructures with rich oxygen vacancies

Hongyu Tang[1], **Chenshan Gao**[2,3], **Huiru Yang**[4,5], **Leandro Sacco**[1], **Robert Sokolovskij**[5,6], **Hongze Zheng**[5,6], **Huaiyu Ye**[5,6,*], **Sten Vollebregt**[1], **Hongyu Yu**[5,6], **Xuejun Fan**[7] and **Guoqi Zhang**[1,*]

[1] Department of Microelectronics, Faculty of Electrical Engineering, Mathematics and Computer Science, Delft University of Technology, Delft 2628 CT, The Netherlands
[2] Key Laboratory of Optoelectronic Technology and Systems, Education Ministry of China; College of Opto-electronic Engineering, Chongqing University, Chongqing 400044, People's Republic of China
[3] Sky Chip Interconnection Technology co., Ltd, Shenzhen 518117, People's Republic of China
[4] Harbin Institute of Technology, Harbin 150001, People's Republic of China
[5] School of Microelectronics, Southern University of Science and Technology, Shenzhen 518055, People's Republic of China
[6] Shenzhen Institute of Wide-bandgap Semiconductors, Shenzhen 518055, Guangdong, People's Republic of China
[7] Department of Mechanical Engineering, Lamar University, TX 77710, United States of America
[*] Authors to whom any correspondence should be addressed.

E-mail: h.ye@tudelft.nL and G.Q.Zhang@tudelft.nl

Keywords: room temperature, ppt-level, NO_2 sensor, SnO_x/SnS heterostructures, oxygen vacancies

Supplementary material for this article is available online

Abstract

In this paper, tin oxidation (SnO_x)/tin-sulfide (SnS) heterostructures are synthesized by the post-oxidation of liquid-phase exfoliated SnS nanosheets in air. We comparatively analyzed the NO_2 gas response of samples with different oxidation levels to study the gas sensing mechanisms. The results show that the samples oxidized at 325 °C are the most sensitive to NO_2 gas molecules, followed by the samples oxidated at 350 °C, 400 °C and 450 °C. The repeatabilities of 350 °C samples are better than that of 325 °C, and there is almost no shift in the baseline. Thus this work systematically analyzed the gas sensing performance of SnO_x/SnS-based sensor oxidized at 350 °C. It exhibits a high response of 171% towards 1 ppb NO_2, a wide detecting range (from 1 ppb to 1 ppm), and an ultra-low theoretical detection limit of 5 ppt, and excellent repeatability at room temperature. The sensor also shows superior gas selectivity to NO_2 in comparison to several other gas molecules, such as NO, H_2, SO_2, CO, NH_3, and H_2O. After x-ray diffraction, x-ray photoelectron spectroscopy, scanning electron microscopy, transmission electron microscope, and electron paramagnetic resonance characterizations combining first principle analysis, it is found that the outstanding NO_2 sensing behavior may be attributed to three factors: the Schottky contact between electrodes and SnO_x/SnS; active charge transfer in the surface and the interface layer of SnO_x/SnS heterostructures; and numerous oxygen vacancies generated during the post-oxidation process, which provides more adsorption sites and superior bandgap modulation. Such a heterostructure-based room-temperature sensor can be fabricated in miniaturized size with low cost, making it possible for large-scale applications.

1. Introduction

Air pollution is a major problem that severely impacts human health and ecosystems around the world. Nitrogen dioxide (NO_2), one of the most abundant air pollutants, is mainly emitted by fossil fuel burning, road traffic, indoor combustion source [1], and biomass burning [2]. The World Health Organization (WHO) recommends an ambient air quality guideline of 40 μg m^{-3} (21 ppb) annual average NO_2 concentrations [3, 4]. With the application of the Internet of Things (IoT), the possibility arises to deploy a grid of sensors based on semiconductor devices to detect multiple sources of pollution, and subsequently wirelessly transmit the collected data in real-time [5–8]. Under this context, many efforts were focused on developing a miniaturized highly sensitive and reversible NO_2 gas sensor with a low limit

of detection (LOD) operating at room temperature [9]. Various high sensitivity NO_2 gas sensors based on metal oxide semiconductors like SnO_2 [10], WO_3 [11], ZnO [12, 13], In_2O_3 [14], V_2O_5 [15], and MoO_3 [16] have been developed. However, their limits of detection are mostly at the ppm-level, and the operating temperature is high (100 °C–300 °C). To realize high working temperature, heaters are mostly integrated with metal oxide-based sensors, which would lead to high power consumption undesired in IoT applications [17, 18].

To overcome the shortcomings of metal oxide-based devices, many groups have developed room-temperature NO_2 gas sensors based on 2D materials or heterostructures constructed with two or more semiconductors [19–23]. The SnO_2–ZnO hybrid nanofibers-based sensor reported by Park *et al* [24] exhibited a high sensing response to NO_2 with a low concentration of 400 ppb at 200 °C. Li *et al* [25] fabricated a sensor based on p–n SnO_2–SnO heterojunctions, which had a LOD of 0.1 ppm NO_2 at a relatively low operating temperature (50 °C). To further reduce operating temperature, junction with metal sulfide has been employed because its narrower bandgap can promote the catalysis of the surface reaction with gas molecules. Cui *et al* [26] reported a SnO_2/MoS_2 hybrids NO_2 gas sensor that has a lower detection limit of 0.5 ppm. Hao *et al* [27] demonstrated that SnS_2/SnO_2 nanocomposites have enhanced NO_2 gas sensing behaviors, which showed a high response of ∼90% towards 125 ppb at 100 °C. As a typical metal sulfide, tin-sulfide (SnS) is a layered material, which has black phosphorus-like puckered structures [28–30]. Due to its anisotropic crystal structures, the charge transfer between polar gases and SnS is strong which leads to outstanding gas sensing properties [31]. SnS nanoflakes have been used for detecting humidity [32], volatile compounds [33], and noxious gas, such as NO_2, acetone, and alcohol [34]. SnS_2/SnS p–n heterojunctions were constructed to detect NO_2 at room temperature, whose LOD is 75 ppb [35]. In addition, the groups of Epifani [10] and Li [36] have proved that SnO_2 with oxygen vacancies (OVs) for NO_2 gas detection exhibited an ultrahigh response at room temperature. They also found that at higher operating temperatures the gas sensing responses are reduced. These previous results indicate that introducing OVs is an efficient way of enhancing gas sensing performance.

Here, we present a high-performance gas sensor using a tin oxidation (SnO_x)/SnS heterostructure that is synthesized by oxidizing pristine SnS in air at different oxidization temperatures and times. Benefiting from the unique nanostructure surface morphology, including the Schottky nature of metal–SnO_x/SnS heterostructure, the heterostructure of SnO_x and SnS, its large area, and the abundances of OVs, the fabricated gas sensor owns a high response, ultra-low theoretical LOD, and high selectivity towards NO_2 while operating at room temperature. The proposed sensor is low-cost and easy to fabricate, which has great potential application in the mass production of miniaturized room-temperature sensors for IoT applications. The gas sensing mechanism can be efficiently recognized by the analysis method combining experiments and density functional theory (DFT) simulations.

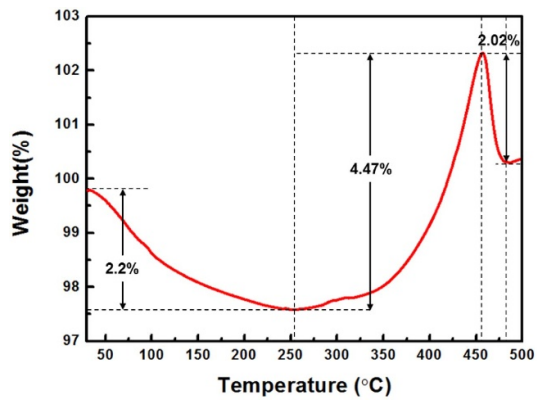

Figure 1. TGA profiles of SnS nanosheets from room temperature to 500 °C in air.

2. Methods

2.1. Preparation of SnS nanosheets

SnS nanosheets are liquid-phase exfoliated (LPE) from SnS powder to obtain a large surface area [37]. The SnS nanomaterial was purchased from six carbon Corp, China. SnS (mg) was mixed with ethanol (ml) thoroughly after stirred the mixture solution for 20 min [38]. The obtained suspensions were ultrasonicated in a KH-500B benchtop ultrasonic bath (250 W) operating at 40 kHz frequency and 100% power for 12 h. The bath temperature was maintained below 30 °C during sonication through a water-cooling coil. The dispersion was then centrifuged at a rate of 500 rpm for 1 h and 10 000 rpm for 35 min sequently to remove the remaining bulk material. The top two-thirds of the supernatant was collected for further process.

2.2. Design and fabrication of gas sensor

Oxidation not only increases the surface area of the functional materials but also introduces many defects during oxidation. For instance, the OVs and step edges are the most reactive sites on the surface of metal oxides. To know the thermal stability of SnS nanosheets in air, TGA is carried out from room temperature to 500 °C in air. The oxidation of SnS to SnO_x occurred through the reaction $SnS + (1 + x/2)\ O_2 \rightarrow SnO_x + SO_2$ $(1/2 < x < 8/3)$ [39]. As shown in figure 1, the weight decreases by 2.2% from room temperature to 252 °C, where the $x = 1.82$. After that, the weight gradually increases again. From 325 °C, the weight increase rapidly, and the $x = 2.18$ in the

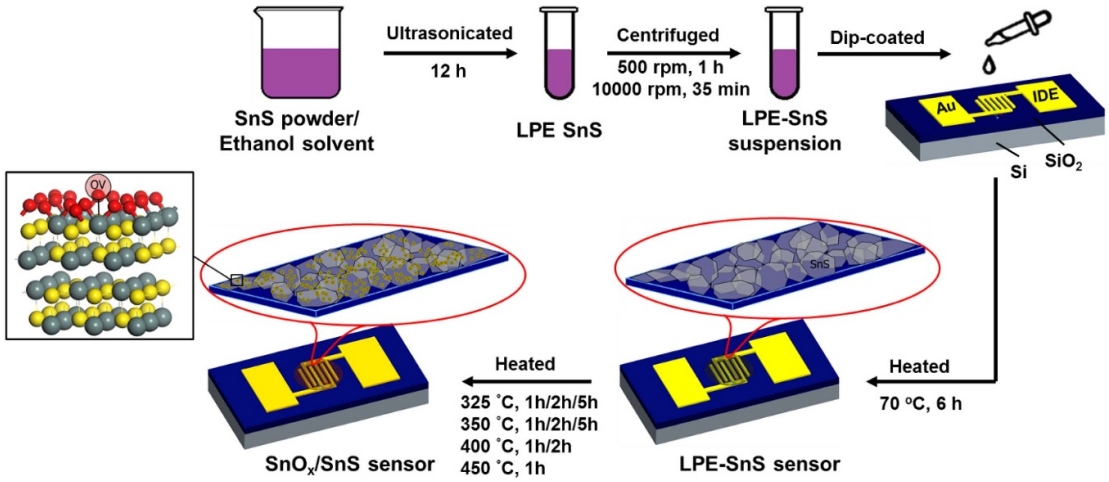

Figure 2. Fabrication process of the SnO_x/SnS heterostructure-based gas sensor.

peak of 450 °C because of the generation of higher oxidation states, e.g. SnO_2 and Sn_3O_8. The weight decreases again from 450 °C, which may be induced by the decomposition of heavy oxides. Since 325 °C and 450 °C are critical temperatures of materials compositions change in SnO_x, we set four temperature levels: 325 °C, 350 °C, 400 °C, and 450 °C. There are nine groups of samples, including oxidized at 325 °C for 1, 2, and 5 h, oxidized at 350 °C for 1, 2, and 5 h, oxidized at 400 °C for 1, 2 h, and oxidized at 450 °C for 1 h. In the present work, gold interdigitated electrodes (IDEs) with electrode width of 10 μm and a gap of 5 μm were fabricated using photolithography technologies before dip coating and the oxidation of SnS nanosheets. After dip coating SnS nanosheets on the IDEs, the SnS-based gas sensors can be obtained by drying at 70 °C for 2 h in air. To fabricate SnO_x/SnS-based gas sensor, we oxidized the SnS-based gas sensor at different oxidization temperatures and times in air, as shown in figure 2.

2.3. Characterizations

The morphologies of the SnO_x/SnS were characterized by a field-emission scanning electron microscopy (FESEM) (JEOL JSM-7610FPlus) using an acceleration voltage of 5 kV with a working distance of 8 mm. The chemical mappings of the SnS nanosheets and SnO_x/SnS heterostructure were also obtained by energy-dispersive x-ray spectroscopy (EDS) (Oxford X-Max^N-50) using an acceleration voltage of 20 kV with a working distance of 10 mm. The crystalline microstructure was characterized by a transmission electron microscope (TEM) (JEOL JEM-2100). The crystal structures of SnS nanosheets and SnO_x/SnS heterostructure were measured by a Bruker D8 x-ray diffraction (XRD) with Cu Kα1 radiation in the 2θ range from 10° to 80°. X-ray photoelectron spectroscopy (XPS) studies were performed with a Thermofisher Nexsa to investigate surface modification. The electron paramagnetic resonance (EPR) plots were recorded by using a Bruker EMX spectrometer operating in the X band frequency at room temperature. The gas sensing performances were measured by a digital controlled gas mixing (dry air and target gas) and data recording systems in real-time. The bias voltage, testing time, and concentration of gases in the chamber were controlled by the computer. The electrical resistance of the sensors was recorded by a source meter (Keithley 2450). The gas sensing responses of devices (S) are defined as the relative change in the resistance of the sensors in the background and those in the tested gas $S = (R_{gas} - R_{air})/R_{air} \times 100\%$, where R_{gas} and R_{air} are the resistance in the tested gases and air, respectively. The response time is defined as the time taken to achieve 90% of the total response of the device. The recovery time is defined as the time required for recovering 90% of the initial value of the gas response.

3. Results and discussion

3.1. Characterization

The crystallographic information of SnS nanosheets and nine types of SnO_x/SnS is confirmed by XRD as shown in figure 3. The structures and stabilities of intermediate compounds, such as Sn_2O_3, Sn_3O_4, and Sn_5O_6, are still open to debate [40, 41]. All samples display peaks at 26°, 27.5°, 30.5°, 31.5°, 32°, 39.3°, 45.5°, 48.5°, 51°, and 66.8° are indexed to the (120), (021), (101), (111), (040), (041), (002), (211), (112) and (080) planes of SnS (JCPDS Card No. 39-0354). All oxidized samples show peaks at 28.6°, 33.9°, 54°, 63.5° corresponding to the (112), (113), (132), (117) planes of SnO (JCPDS Card No. 77-2296), peaks at 26.6°, 51.8° from the (110), (211) planes of SnO_2 (JCPDS Card No. 41-1445), peaks at 21.8°, 25.8° from the (020), (011) planes of Sn_2O_3 (JCPDS Card

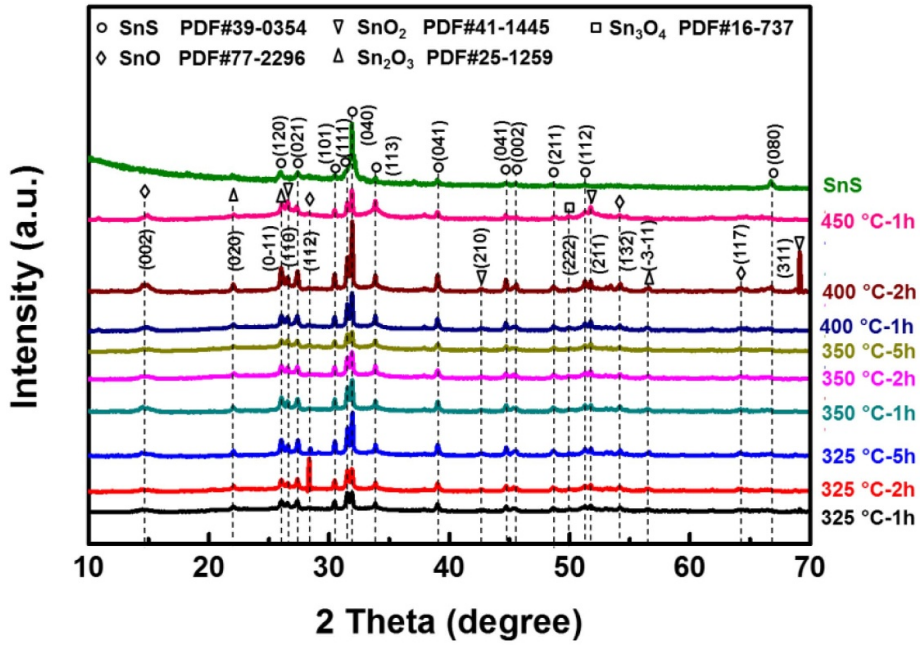

Figure 3. X-ray diffraction patterns of the as-synthesized samples.

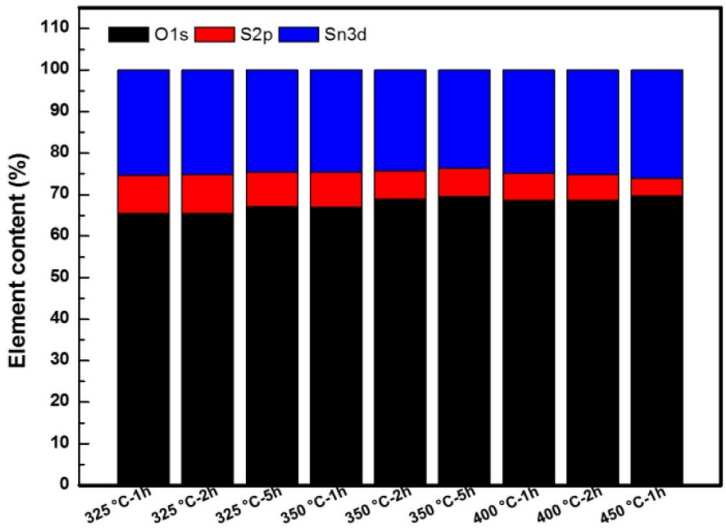

Figure 4. Element content of the as-synthesized samples.

No. 25-1259), and peaks at 15°, 50.1° from the (010), (222) planes of Sn_3O_4 (JCPDS Card No. 16-737), respectively. It indicates that all samples have SnO, SnO_2, Sn_2O_3, Sn_3O_4, and SnS, while the content is different due to the different intensity of each peak. For instance, the samples oxidized at 325 °C display a high-intensity peak at from the (112) plane of SnO; some peaks at (117) of SnO, (210) of SnO_2, and (311) of Sn_2O_3, disappear from the XRD pattern of 450 °C samples.

To accurately evaluate the element content of each SnO_x/SnS heterostructures, XPS images are employed to show their chemical states and chemical composition (figures 4 and 5). As shown in figure 4, the oxygen content increases as the temperature increases. The longer the oxidation time, the higher the oxygen content. The 450 °C sample has the highest oxygen content, 61%. Furthermore, figure S1(a) (available online at stacks.iop.org/2DM/8/045006/mmedia) shows the deconvolution of the Sn 3d spectra, the peaks at 486.8 and 495.0 eV are ascribed to the Sn $3d_{5/2}$ and Sn $3d_{3/2}$ of Sn^{2+} species [42, 43], respectively, while the binding energies at 487.3 and 495.7 eV correspond to the Sn $3d_{5/2}$ and Sn $3d_{3/2}$ of Sn^{4+} species [42, 44, 45]. The O 1s spectrum is fitted with two peaks at 530.7 and 531.9 eV, corresponding to the O–Sn^{2+} and O–Sn^{4+} groups, respectively (figure S1(b)) [46, 47]. The S 2p spectrum can be split into four peaks at 161.4, 162.7,

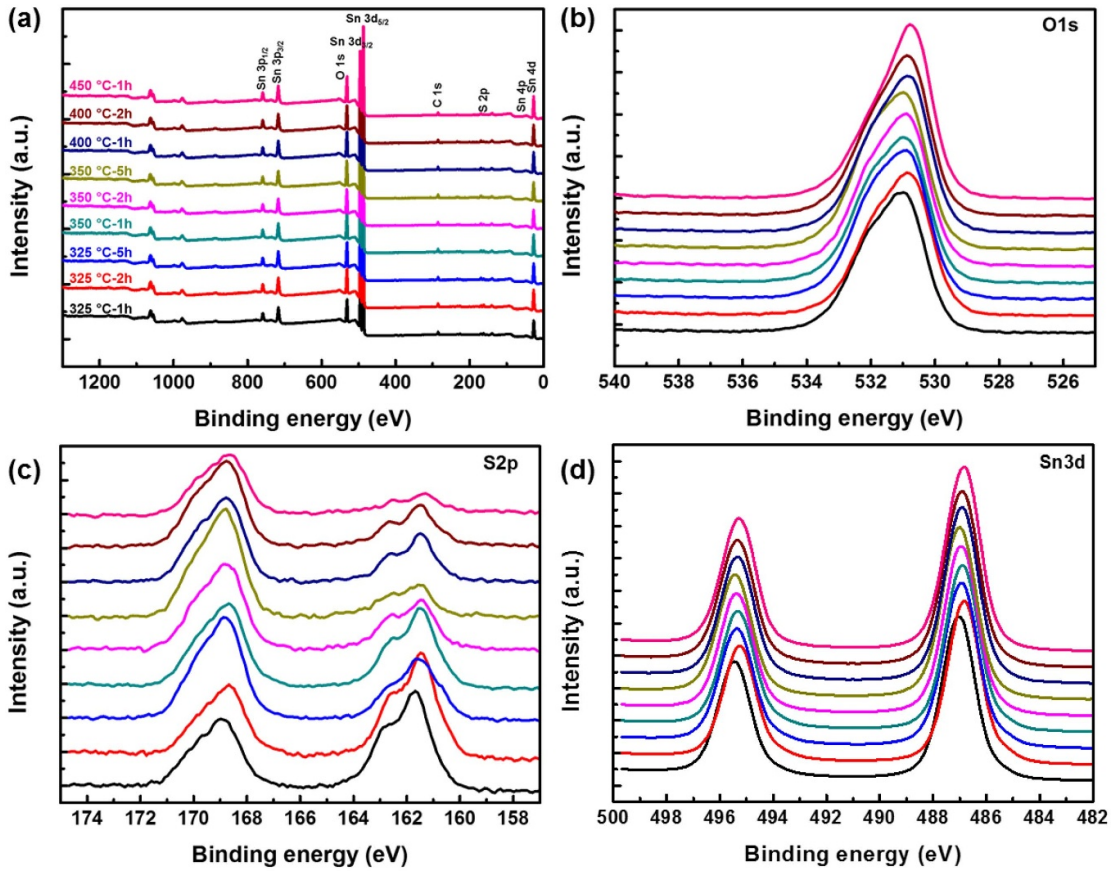

Figure 5. XPS curves of nine types SnO_x/SnS samples. (a) The survey spectra of the samples. (b) The oxygen core level (O 1s) spectra of the samples, (c) score level (S 2p) spectra of the samples, (d) the Sn core level (3d) of the samples.

168.7, and 169.9 eV, which are ascribed to the S $2p_{3/2}$ and $2p_{1/2}$ peaks (figure S1(c)) [48].

Figure 6 shows the EPR results, which reveals that there are symmetrical resonance lines in the spectra located at $g \approx 2.00$ in SnO_x/SnS and SnS nanosheets samples, which is assigned as surface superoxide centers Sn^{4+}–O_2^-. The electrons are trapped in OVs, and then transfer between the surface adsorbed O_2 molecule in SnO_2, and finally formed surface superoxide centers ($Sn^{4+} + V_O^- + O_2 \leftrightarrow Sn^{4+}$–$O_2^-$). The superoxide radicals are firmly attached to Sn^{4+} or Sn^{2+} species on the surface, increasing adsorption sites for gas molecules [36, 49]. After LPE and 70 °C annealing process, there are few vacancies on the surface of SnS. It is seen that the intensity of signals in the samples of 325 °C and 350 °C are much stronger than those observed in 400 °C and 450 °C. It indicates that it is a relatively much larger oxygen deficiency in 325 °C and 350 °C.

3.2. Gas sensing performances

3.2.1. The effects of UV light on the gas sensing performance

Figure 7(a) shows the test set-up for SnO_x/SnS heterostructure-based gas sensor. To analyze the effect of UV irradiation on gas sensitivity, we compared and analyzed the gas response of 350 °C-1 h samples under different UV illumination conditions. The first one is applying UV light (1.3 W UV lamp with 365 nm wavelength, light intensity is 19 mW cm^{-2}) from gas in to gas out, the second one is setting dark from gas in to gas out, the third one is applying UV light only for the recovery process. To make a quick comparison, we set 100 ppb NO_2 gas in for 15 min and gas out for 15 min, respectively. In this paper, the 'baseline' is defined as the response value that when the device recovers to stability after each injection of dry air (the response value before injecting NO_2 gas is also included). The higher the slope of baseline, the larger it shifts. As shown in figure 7(b), in the case of full darkness, the device cannot be recovered to the initial state, and the baseline is severely shifted (see figure S2(b)); in the case of full UV illumination, the response and recovery speed are very fast, but the responsivity is low. Obviously, the device with UV illumination only in the recovery process has a high gas response as well as a fast recovery time. Therefore, the gas responses in this work were tested in this mode.

3.2.2. The effect of oxidation content on gas sensing performances

From the previous analysis results, it is found that different oxidation temperatures and oxidation times

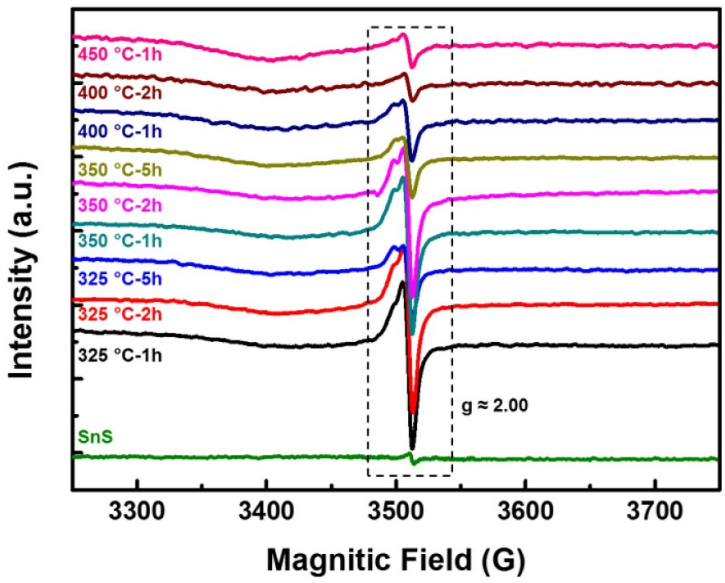

Figure 6. EPR spectra comparison of SnS nanosheets and SnO_x/SnS heterostructure.

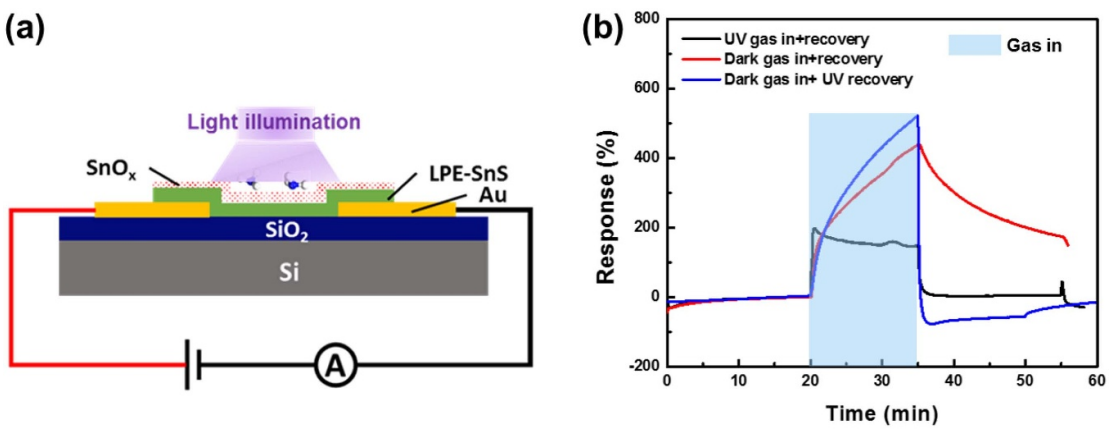

Figure 7. (a) Schemitic test setup of SnO_x/SnS heterostructure-based gas sensor. (b) Dynamic response of SnO_x/SnS gas sensor toward 100 ppb NO_2 gas concentration at room temperature (25 °C). Gas in for 15 min, gas out for 15 min.

can generate different proportions of oxygen element content and form different OVs. Thus we conducted gas response tests for each group of SnO_x/SnS heterojunctions. To make a quick comparison, we set 3 ppm NO_2 gas in for 10 min and gas out for 10 min, respectively. As shown in figure 8, it is found that the samples oxidized at 325 °C have the highest gas response among all samples while the shift of baseline is large; the gas responses of samples oxidized at 350 °C are lower than that of samples oxidized at 325 °C but much higher than that of samples oxidized at 400 °C and 450 °C. Moreover, the repeatability of samples created at 350 °C is much better than the other fabricated samples, and there is almost no shift in the baseline. Thus, we systematically analyze the gas responses and gas sensing mechanism for the samples oxidized 1 h at 350 °C.

3.2.3. Gas sensing performances of the 350 °C-1 h SnO_x/SnS gas sensor

The current-voltage (IV) curves of pure SnS-based and 350 °C-1 h SnO_x/SnS heterostructure-based gas sensors are shown in figure 9(a), which reveals that the conductivity of the device increases after oxidation. Moreover, it shows the rectifying output characteristics, indicating a Schottky contact between the sensing materials and the electrodes. Figure S2(a) shows that the lower the operating temperature the higher the gas response, which is attributed to rich OVs according to the previous work [10, 36]. In figure S2(b), the resistance changes of SnS and SnO_x/SnS sensors toward different NO_2 gas concentrations were measured under two conditions: without UV and with UV illumination at the recovery phase only. To recover to the initial value, we applied UV illumination for the first 15 min, and then in dark for 15 min

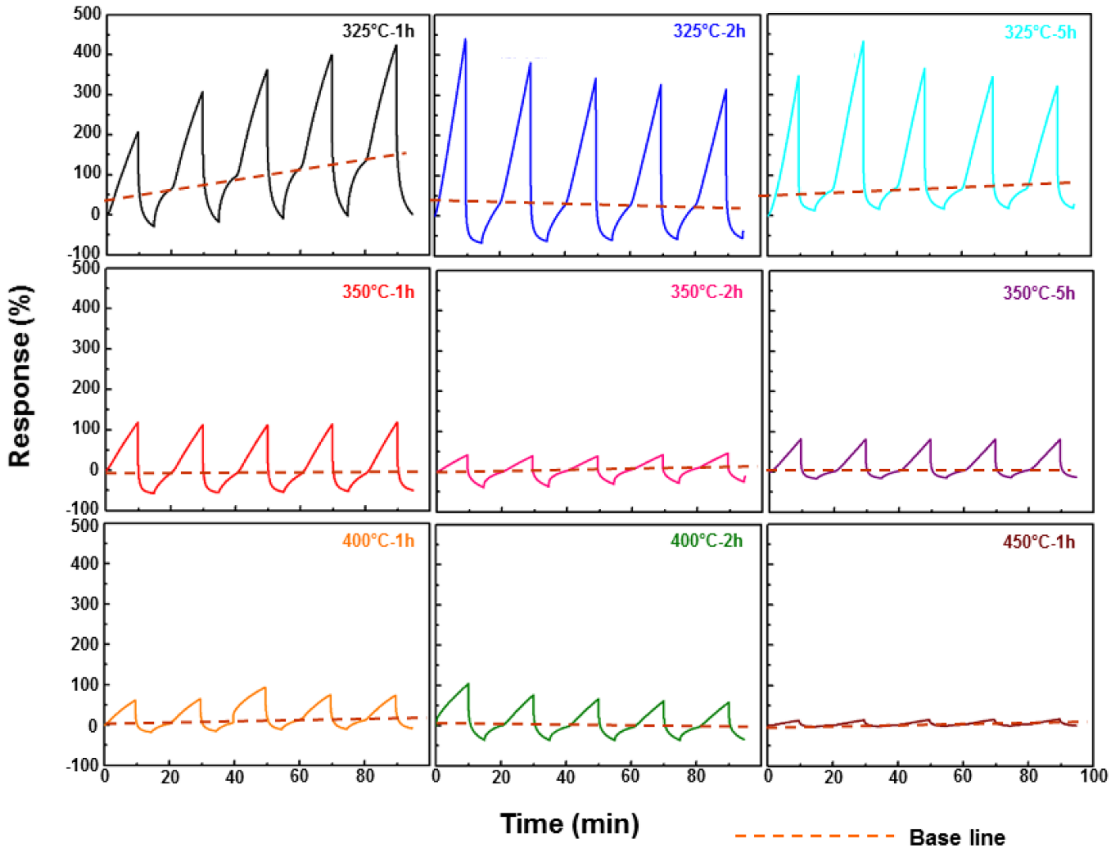

Figure 8. Dynamic response of nine types of SnO_x/SnS gas sensor toward 3 ppm NO_2 gas concentration at room temperature. Gas in for 10 min, gas out for 10 min.

remaining. Figure 9(b) shows five cycles of measurements of SnS nanosheets-based and SnO_x/SnS heterostructures-based gas sensors. It is found that the repeatability of them is good, and the response of the SnO_x/SnS device is much higher than that of the SnS device. The superior gas sensing performance is determined by the large amount of Sn^{4+}–O_2^- centers in the heterostructures. Figure 9(c) shows the dynamic sensing performance of 350 °C-1 h sample detected from 1 ppb to 1 ppm gas concentrations. It notes that the recovery time of gas sensors after applying UV illumination is only 36 s, which is much faster than that of most SnO_2-based sensors (SnO_2 modified carbon nanotubes (CNTs), 408 s @ 100 ppb, and SnO_2 NPs, 2400 s @ 100 ppb) [10, 50].

Figure 9(d) illustrates the responses of SnO_x/SnS heterostructures as a function of the NO_2 concentrations range from 1 ppb to 1 ppm. The fitted experimental data shows an exponential relationship with the gas concentration of NO_2 (C), as Response (S) $= 83.24 \times C^{0.34}$. The inset image of figure 9(d) shows the linear fitting $\log(S) - \log(C)$ plot, revealing a Freundlich adsorption relation between the NO_2 molecules and SnO_x/SnS heterostructure, which is the most important multisite adsorption isotherm for rough surfaces [51]. Moreover, our device exhibits a response of ≈171% to the 1 ppb NO_2 (lower concentrations cannot be reached due to limitations imposed by our gas mixture system). It is much lower than the recommended ambient air quality guidelines of WHO (20 ppb). As shown in figure S3 and tables S1, S2, the signal of the as-fabricated sensor is three times more than the noise (0.39×10^{-3}), thus the theoretical LOD can be calculated according to the International Union of Pure and Applied Chemistry [52, 53]. The LOD is as low as 5 ppt, which is much lower than that of carbon nanotubes-based, metal oxide-based, and metal sulfide-based sensors (see table 1)[25, 35, 54–58].

Furthermore, we investigated the selectivity of the sensors in air for finding more practical application capability (see figure S5). The responses of the SnO_x/SnS heterostructures-based device toward other gases, including NH_3, H_2, NO, CO, and SO_2 were measured. With the gas concentration of 500 ppm, the sensor response toward NO and CO are 377% and 181%, respectively, while for NH_3 and H_2 are −63% and −55%, respectively. The sensor shows response of 47% towards 1 ppm SO_2. Besides, it shows a response of −700% at 11% relative humidity (RH) and high response of −10 870% at 75% RH. Thus it is known that SnO_x/SnS gas sensors have high selectivity at low RH environments. Therefore, the SnO_x/SnS heterostructure is an ideal sensing platform with excellent selectivity, response, reversibility, ultra-low LOD, and low operating temperature.

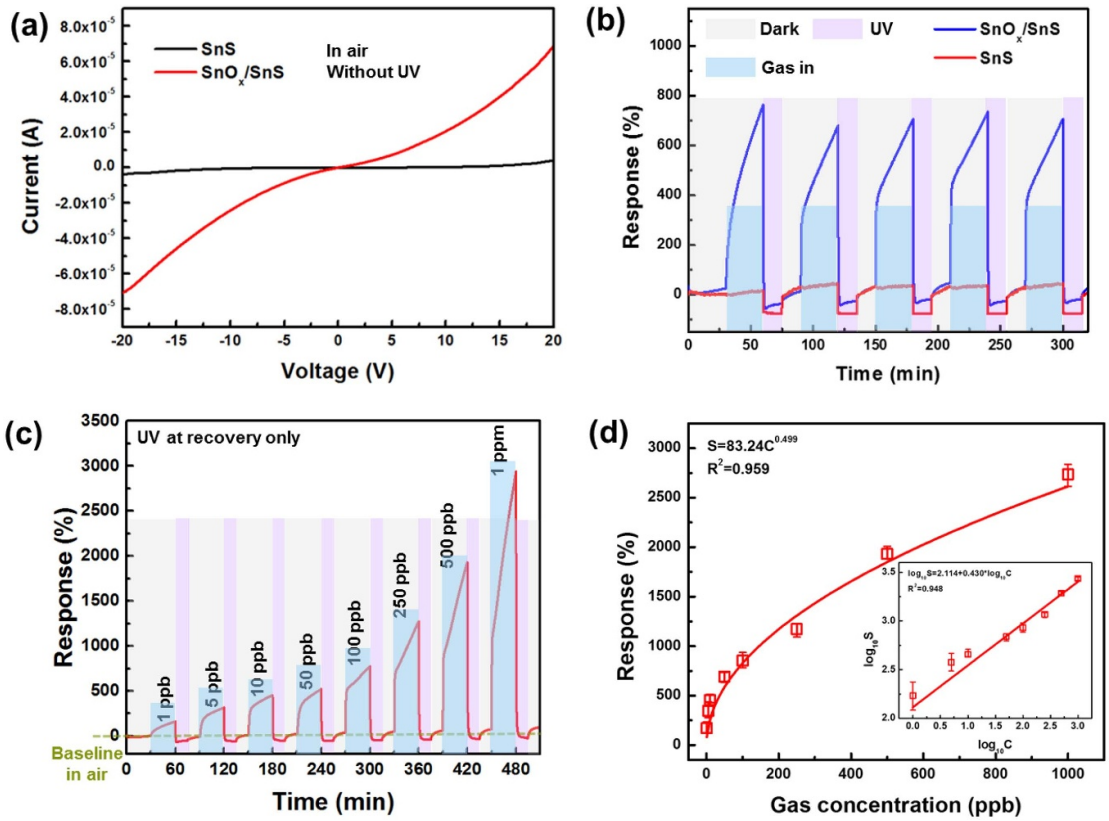

Figure 9. (a) *I–V* curve of SnS-based and 350 °C-1 h SnO_x/SnS heterostructures-based gas sensor measured at room temperature in air. (b) Time-dependent response current of five cycles of NO_2 gas switching between the air and 100 ppb. (c) Dynamic sensing performance of 350 °C-1 h sample under different gas concentrations. (d) The sensor response as a function of the concentration of NO_2 gas. (The bias voltage is 10 V.).

Table 1. Comparison of various gas sensor technologies with respect to reported NO_2 ranges, operating temperature, response and recovery times, and response.

Sensing materials	C(NO_2) (ppb)	LOD (ppb)	Temperature (°C)	Response time (s)	Recovery time (s)	Response (%)	Reference
WO_3	500	10	200	∼3600	∼1800	150	[58]
HOF	100	40	25	17.6	19.1	∼6.9	[57]
CNT	1	0.1	25	120	—	∼25	[59]
SnO_2	1	0.2	25	∼1800	∼900	∼90	[56]
SnO_2–SnO	100	100	50	∼150	∼400	26 ppm^{-1}	[25]
SnO_2–ZnO	400	—	200	∼300	∼300	600	[24]
SnO_2/graphene	10	0.024	150	43	408	200–300	[55]
MoS_2/SnO_2	500	—	25	408	162	0.6	[26]
SnS_2/SnO_2	125	—	100	299	143	∼90	[27]
SnS_2	10 000	—	120	∼170	∼140	∼3600	[60]
SnS	1000	—	25	∼25	∼25	60	[34]
SnS_2/SnS	400	75	25	365	1216	660	[35]
SnO_x/SnS	1 1000	0.005	25	1800	36 (UV)	171 2735	This work

CNT: carbon nanotube, HOF: hydrogen-bonded organic framework material.

3.2.4. Gas sensing mechanism

The possible gas sensing mechanism of SnO_x/SnS heterostructure-based sensors are the Schottky nature of SnO_x/SnS–metal contact, SnO_x and SnS heterostructures, and OVs. The SEM (figure 10(a)) in combination with EDS elemental mapping shown in figure S2 reveals that there are O, S, and Sn elements in the SnO_x/SnS heterostructure, and all of them are uniformly distributed, further confirming the existence and uniform distribution of SnO_x nanoparticles in the SnS nanosheets. The TEM images (figures 10(b) and (c)) show that the fringe interval of 0.292 nm corresponds to the d-spacing of (101) SnS, meanwhile, the fringe interval of 0.334 and 0.176 nm agrees well with the d-spacing of (011) and (211) crystal planes of SnO_2, respectively. The fringe interval of

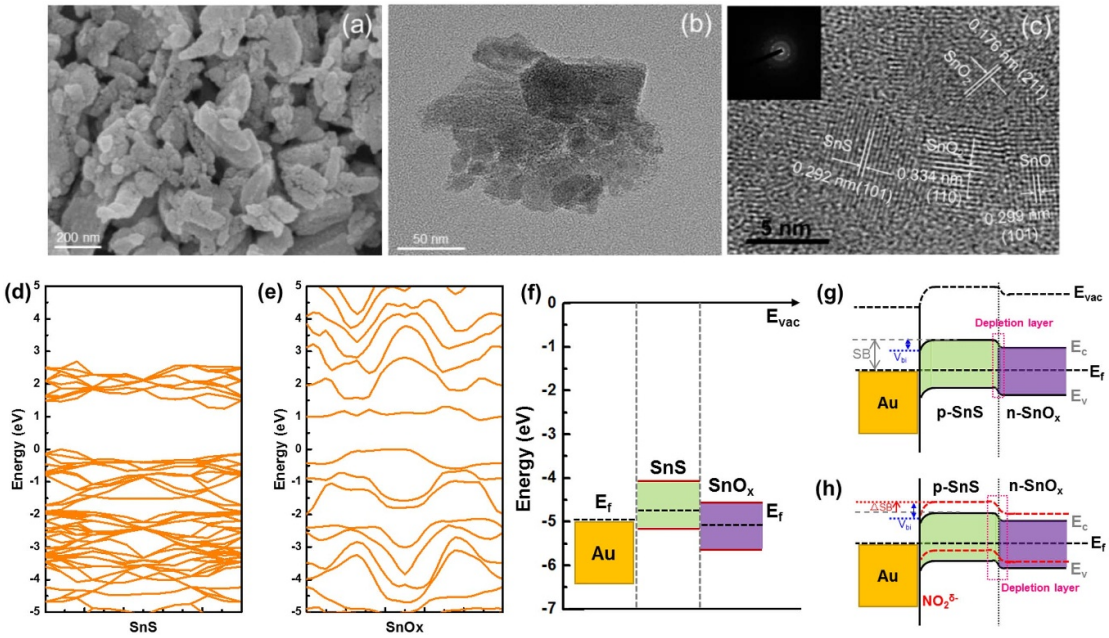

Figure 10. SEM characterization of (a) SnO_x/SnS heterostructures, TEM image of (b) SnO_x/SnS heterostructures, high-resolution TEM (HRTEM) image of (c) SnO_x/SnS heterostructures, the inset images is selected area electron diffraction (SAED) rings. Band structure of (d) SnS and (e) SnO_x with first-principles calculations. (f) Calculated band alignment between SnS and SnO_x, and the position of the work function of Au. The black dashed lines represent the Fermi level, which is a Schottky contact. Energy band structure of the SnO_x/SnS heterojunction contact with Au in (g) air and (h) a NO_2 atmosphere.

0.299 nm corresponds to the d-spacing of (101) SnO. DFT calculations were conducted to study the band structure of SnS, SnO_x, and SnO_x/SnS, the charge transfer and energy distribution between NO_2 gas molecule and SnO_x/SnS heterostructures. The oxidation process between the top SnS layer and the O_2 gas molecule in the unit cell are shown in figure S6.

The calculated band structures of SnS and SnO_x are shown in figures 10(d) and (e). The band structure provides the bandgap values of metal electrodes, SnS, and SnO_x (see figure 10(f)). The work function of Au and SnS are 5.1 and 4.88 eV, respectively [44]. Thus, it is Schottky contact between Au and SnS. The surface of SnS is free from Fermi level pinning, thus the Schottky barrier height (SBH) of the device can follow the trend of the Schottky–Mott limit [61]. The SBH is equal to the sum of the bandgap of SnS (E_g) and electron affinity (χ) minus the work function of the metal (W_M). NO_2 absorption moves the Fermi level (E_f) toward the valence band (E_v), increases the build-in potential (V_{bi}), consequently shifts the Schottky barrier (SB) by ΔSB, and decreases the device current (see figures 10(g) and (h)).

Based on the first principle analysis results, it is found that SnS and SnO_x are p-type and n-type semiconductors respectively. The response of the SnO_x/SnS-based sensor is much higher than that of SnS, because of the formed heterojunction between SnS and SnO_x, and the numerous defective microstructures (e.g. OVs) at the surface of SnO_x. Figures 10(g) and (h) shows the band diagrams of SnS and SnO_x before and after equilibrium, which reveals a higher E_f of SnS compared to that of SnO_x. Therefore, electrons flow from the SnS to the SnO_x can induce the energy band bending in the depletion region at the interface between them [62]. When the sensor is in air, oxygen species are adsorbed on the surface and the interface layer of SnO_x/SnS, the extraction of the electrons from the E_c can form ionic oxygen species (O_2^- or O^-). When NO_2 is introduced, the NO_2 molecules react with ionic oxygen species and trap electrons from the heterostructures, produce NO_3^- or NO_2^-. Due to the non-equilibrium built-in electric field, extra electrons slip from SnS to SnO_x, inducing a wider depletion layer and the decreased conductivity of the device consequently.

According to the EPR results, it is known that it is a much larger oxygen deficiency in the samples of 325 °C and 350 °C, thus the NO_2 gas responses are higher than in other samples. In order to further investigate the effects of OVs, we analyze the adsorption energy (E_A) and change transfer (ΔQ) of NO_2 on SnO_x/SnS heterojunction with OVs, which are −0.314 eV and −0.283 e, respectively. The charge density difference CDD presented in figure 11(b) confirms that NO_2 acts as a charge acceptor with a larger charge transfer. The bandgap before and after adsorbed NO_2 is 0.037 and 0.219 eV, respectively. According to the classical relation between E_g and electrical conductivity (σ) of materials [63], $\sigma \propto e^{(-Eg/2kT)}$, where k and T are the Boltzmann's constant and the temperature respectively. Thus the resistance increases when the gas sensor is exposed to the NO_2 gas molecules. Furthermore, ELF plots in figure 11(c) show that few electrons share between NO_2 gas molecules and substrates (SnS, SnO_x/SnS),

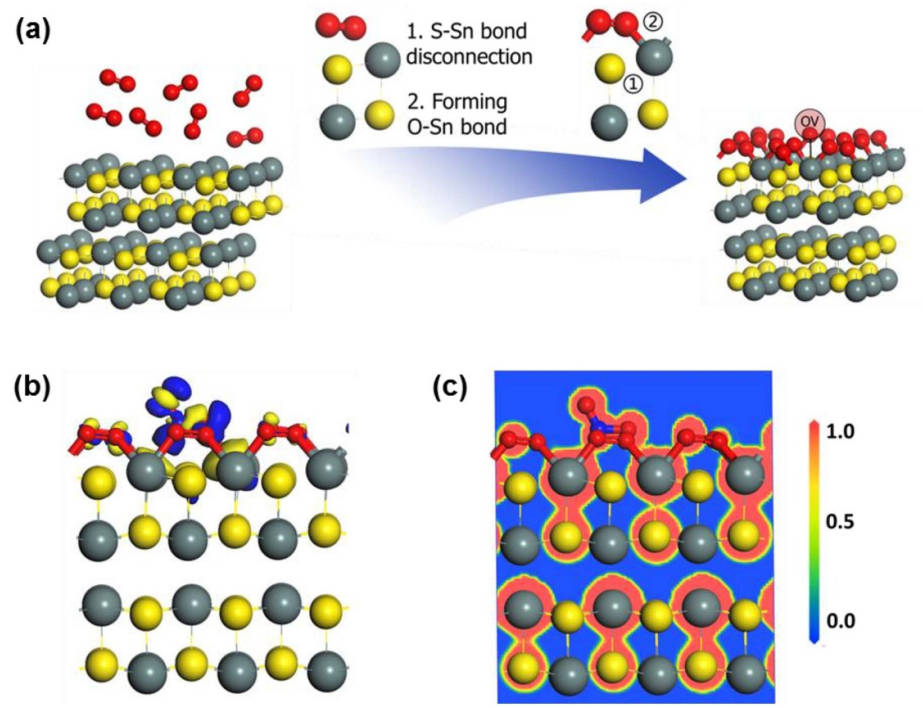

Figure 11. (a) The formation of OV-rich SnO_x/SnS heterostructure. The charge density difference (CDD) plots for NO_2 on (b) SnO_x/SnS heterostructure. The blue and yellow regions show charge accumulation and depletion, respectively. The electron localization function (ELF) plots for NO_2 on (c) SnO_x/SnS heterostructure. The isosurface is taken as 0.015 e $Å^{-3}$.

which proves a chemical adsorption nature. Thus NO_2 gas molecule is difficult to be desorbed from the surface of SnO_x/SnS heterostructures, inducing a long recovery time, as shown in figure 7(b).

Therefore, UV irradiation was applied during the desorption (recovery) process in the gas sensing measurement. The ultra-narrow bandgap of SnO_x/SnS heterostructures with OVs means that the photoinduced electrons can transfer from the valence band to the conduction band much easily. It leads to the absorption of more photons in the UV light ($\lambda = 365$ nm) to produce more electron–hole pairs, resulting in more O_2^- and NO_2^- is photoexcited to be O_2 and NO_2 [64, 65]. Finally, it accelerates the gas desorption from the surface of SnO_x/SnS. If we apply UV light for the gas in and recovery process, NO_2 first absorbs UV light and then decomposes into NO and an O_2. The O_2 generated by this reaction can also combine with molecular O_2 to form O_3. Due to the products of these two reactions (NO and O_3), the response of the sensor is reduced according to the selectivity results in figure S6. Therefore, as mentioned before, the response of UV light for the gas in and recovery process is weak.

4. Conclusions

In this work, SnO_x/SnS heterostructures with large surface area and rich OVs were synthesized by the post-oxidation of LPE-SnS nanosheets in air at different oxidation levels. The gas response of the samples oxidized at 350 °C are lower than that of samples oxidized at 325 °C but much higher than that of samples oxidized in 400 °C and 450 °C. The 350 °C-1 h samples exhibit excellent sensing performance with a high response of 171% at 1 ppb and 2735% at 1 ppm NO_2 gas concentration, respectively, excellent repeatability, selectivity, ultra-low theoretical LOD of 5 ppt, and a wide detecting range from 1 ppb to 1 ppm at low humidity environment. Through XRD, XPS, SEM, TEM, and EPR characterizations and first principle analysis, the heterostructures with OVs contribute a large response to the gas molecules possibly due to the Schottky nature of metal–SnO_x/SnS, a large number of adsorption sites, bandgap modulation, and active electrons transfer in the sensing interface layer. The EPR results reveal that the intensity of signals in the samples of 325 °C and 350 °C are much stronger than those observed in 400 °C and 450 °C, indicating higher content of OVs in 325 °C and 350 °C. Thus the samples of 325 °C and 350 °C have higher gas responses. However, NO_2 is chemisorbed on the surface of SnO_x/SnS heterostructures with OVs, the more OVs on the surface of samples, the more difficult to desorb gas molecules. Thus the gas response of 325 °C samples are hard to recover to the initial state. Both experimental and DFT simulation results support that these factors conduce to the superior gas sensing properties in terms of higher sensitivity and ultra-low theoretical LOD toward ppt-level NO_2 at room operating temperature. UV illumination is applied during the recovery process to accelerate recovery time. This study provides a new and low-cost

approach for highly sensitive ppb-level gas detection and can extend to other nanomaterials.

Data availability statement

The data generated and/or analyzed during the current study are not publicly available for legal/ethical reasons but are available from the corresponding author on reasonable request.

Acknowledgments

We thank Dr Zhen Cui in EEMCS of Delft University of Technology for his helpful discussion of simulation. We also thank Dr Anne Doerr in TNW of Delft University of Technology for her vigorous help of SnS nanosheets centrifugation and drying. This work was supported by the National Key R&D Program of China (2018YFE0204600), the Key-Area Research and Development Program of GuangDong Province (2019B010131001), and the Shenzhen Fundamental Research Program (JCYJ20200109140822796).

Conflict of Interest

The authors declare no conflict of interest.

ORCID iDs

Hongyu Tang https://orcid.org/0000-0002-2720-6709
Chenshan Gao https://orcid.org/0000-0002-7425-6573
Leandro Sacco https://orcid.org/0000-0002-5384-2020
Robert Sokolovskij https://orcid.org/0000-0003-0447-9672
Huaiyu Ye https://orcid.org/0000-0002-0385-4728
Sten Vollebregt https://orcid.org/0000-0001-6012-6180

References

[1] Spicer C W, Kenny D V, Ward G F and Billick I H 1993 Transformations, lifetimes, and sources of NO_2, HONO, and HNO_3 in indoor environments *Air Waste* **43** 1479–85
[2] Afzal A, Cioffi N, Sabbatini L and Torsi L 2012 NO*x* sensors based on semiconducting metal oxide nanostructures: progress and perspectives *Sens. Actuators* B **171–2** 25–42
[3] Organization W H 2006 *WHO Air Quality Guidelines for Particulate Matter, Ozone, Nitrogen Dioxide and Sulfur Dioxide: Global Update 2005: Summary of Risk Assessment* (Geneva: World Health Organization)
[4] Goudarzi G R, Mohammadi M J, Ahmadi A K, Neisi A, Babaei A A, Mohammadi B, Soleymani Z and Geravandi S 2012 Estimation of health effects attributed to NO_2 exposure using airQ model
[5] Pham T, Li G, Bekyarova E, Itkis M E and Mulchandani A 2019 MoS_2-based optoelectronic gas sensor with sub-parts-per-billion limit of NO_2 gas detection *ACS Nano* **13** 3196–205
[6] Song C, Yun J, Lee H, Park H, Jeong Y R, Lee G, Kim M S and Ha J S 2019 A shape memory high-voltage supercapacitor with asymmetric organic electrolytes for driving an integrated NO_2 gas sensor *Adv. Funct. Mater.* **29** 1901996
[7] Gillespie-Bennett J, Pierse N, Wickens K, Crane J and Howden-Chapman P 2011 The respiratory health effects of nitrogen dioxide in children with asthma *Eur. Respir. J.* **38** 303
[8] Tang H, Sacco L N, Vollebregt S, Ye H, Fan X and Zhang G 2020 Recent advances in 2D/nanostructured metal sulfide-based gas sensors: mechanisms, applications, and perspectives *J. Mater. Chem.* A **8** 24943–76
[9] David B, Nicola Charlotte Grant B, Eli C, Christos M, Melanie H and Olga K 2020 Frontiers of graphene and 2D material-based gas sensors for environmental monitoring *2D Mater.* **7** 032002
[10] Epifani M, Prades J D, Comini E, Pellicer E, Avella M, Siciliano P, Faglia G, Cirera A, Scotti R and Morazzoni F 2008 The role of surface oxygen vacancies in the NO_2 sensing properties of SnO_2 nanocrystals *J. Phys. Chem.* C **112** 19540–6
[11] Shendage S, Patil V, Vanalakar S, Patil S, Harale N, Bhosale J, Kim J and Patil P 2017 Sensitive and selective NO_2 gas sensor based on WO_3 nanoplates *Sens. Actuators* B **240** 426–33
[12] Yuan H *et al* 2019 ZnO nanosheets abundant in oxygen vacancies derived from metal-organic frameworks for ppb-level gas sensing *Adv. Mater.* **31** 1807161
[13] An W, Wu X and Zeng X C 2008 Adsorption of O_2, H_2, CO, NH_3, and NO_2 on ZnO nanotube: a density functional theory study *J. Phys. Chem.* C **112** 5747–55
[14] Xu P, Cheng Z, Pan Q, Xu J, Xiang Q, Yu W and Chu Y 2008 High aspect ratio In_2O_3 nanowires: synthesis, mechanism and NO_2 gas-sensing properties *Sens. Actuators* B **130** 802–8
[15] Mane A, Suryawanshi M, Kim J and Moholkar A 2017 Fast response of sprayed vanadium pentoxide (V_2O_5) nanorods towards nitrogen dioxide (NO_2) gas detection *Appl. Surf. Sci.* **403** 540–50
[16] Mane A and Moholkar A 2017 Orthorhombic MoO_3 nanobelts based NO_2 gas sensor *Appl. Surf. Sci.* **405** 427–40
[17] Korotcenkov G 2007 Metal oxides for solid-state gas sensors: what determines our choice? *Mater. Sci. Eng.* B **139** 1–23
[18] Wu M, Kim C-H, Shin J, Hong Y, Jin X and Lee J-H 2017 Effect of a pre-bias on the adsorption and desorption of oxidizing gases in FET-type sensor *Sens. Actuators* B **245** 122–8
[19] Park S, An S, Mun Y and Lee C 2013 UV-enhanced NO_2 gas sensing properties of SnO_2-core/ZnO-shell nanowires at room temperature *ACS Appl. Mater. Interfaces* **5** 4285–92
[20] Tang H *et al* 2019 Ultra-high sensitive NO_2 gas sensor based on tunable polarity transport in CVD-WS2/IGZO p-N heterojunction *ACS Appl. Mater. Interfaces* **11** 40850–9
[21] Perrozzi F, Emamjomeh S M, Paolucci V, Taglieri G, Ottaviano L and Cantalini C 2017 Thermal stability of WS_2 flakes and gas sensing properties of WS_2/WO_3 composite to H_2, NH_3 and NO_2 *Sens. Actuators* B **243** 812–22
[22] Black N C G, Liu C G, Pearce R, Li B, Maier S A, Cohen L F, Gallop J C and Hao L 2017 Graphene gas sensing using a non-contact microwave method *Nanotechnology* **28** 395501
[23] Black N C G, Rungger I, Li B, Maier S A, Cohen L F, Gallop J C and Hao L 2018 Adsorption dynamics of CVD graphene investigated by a contactless microwave method *2D Mater.* **5** 035024
[24] Park J-A, Moon J, Lee S-J, Kim S H, Chu H Y and Zyung T 2010 SnO_2–ZnO hybrid nanofibers-based highly sensitive nitrogen dioxides sensor *Sens. Actuators* B **145** 592–5
[25] Li L, Zhang C and Chen W 2015 Fabrication of SnO_2–SnO nanocomposites with p–n heterojunctions for the low-temperature sensing of NO_2 gas *Nanoscale* **7** 12133–42
[26] Cui S, Wen Z, Huang X, Chang J and Chen J 2015 Stabilizing MoS_2 nanosheets through SnO_2 nanocrystal decoration for high-performance gas sensing in air *Small* **11** 2305–13
[27] Hao J, Zhang D, Sun Q, Zheng S, Sun J and Wang Y 2018 Hierarchical SnS_2/SnO_2 nanoheterojunctions with increased active-sites and charge transfer for ultrasensitive NO_2 detection *Nanoscale* **10** 7210–7

[28] Rodin A S, Gomes L C, Carvalho A and Castro Neto A H 2016 Valley physics in tin (II) sulfide *Phys. Rev.* B **93** 045431
[29] Hanakata P Z, Carvalho A, Campbell D K and Park H S 2016 Polarization and valley switching in monolayer group-IV monochalcogenides *Phys. Rev.* B **94** 035304
[30] Tian Z, Guo C, Zhao M, Li R and Xue J 2016 Two-dimensional SnS: a phosphorene analogue with strong in-plane electronic anisotropy *ACS Nano* **11** 2219
[31] Hu F, Tang H, Tan C, Ye H, Chen X and Zhang G 2017 Nitrogen dioxide gas sensor based on monolayer SnS: a first-principle study *IEEE Electron Device Lett.* **38** 983–6
[32] Tang H, Li Y, Ye H, Gao C, Tao L-Q, Tu T, Gou G, Chen X, Fan X and Ren T-L 2019 High-performance humidity sensor using Schottky-contacted SnS nanoflakes for noncontact healthcare monitoring *Nanotechnology* **31** 055501
[33] Afsar M F, Rafiq M A and Tok A I Y 2017 Two-dimensional SnS nanoflakes: synthesis and application to acetone and alcohol sensors *RSC Adv.* **7** 21556–66
[34] Wang J, Lian G, Xu Z, Fu C, Lin Z, Li L, Wang Q, Cui D and Wong C Interfaces 2016 Growth of large-size SnS thin crystals driven by oriented attachment and applications to gas sensors and photodetectors *ACS Appl. Mater. Interfaces* **8** 9545–51
[35] Sun Q, Wang J, Hao J, Zheng S, Wan P, Wang T, Fang H and Wang Y 2019 SnS_2/SnS p–n heterojunctions with an accumulation layer for ultrasensitive room-temperature NO_2 detection *Nanoscale* **11** 13741–9
[36] Li Y, Zu B, Guo Y, Li K, Zeng H and Dou X 2016 Surface superoxide complex defects-boosted ultrasensitive ppb-level NO_2 gas sensors *Small* **12** 1420–4
[37] Brent J R, Lewis D J, Lorenz T, Lewis E A, Savjani N, Haigh S J, Seifert G, Derby B and O'Brien P 2015 Tin(II) Sulfide (SnS) nanosheets by liquid-phase exfoliation of herzenbergite: iv–vi main group two-dimensional atomic crystals *J. Am. Chem. Soc.* **137** 12689–96
[38] Tang H, Qu Z, Wang L, Ye H, Fan X and Zhang G 2019 Liquid-phase exfoliated SnS as a semiconductor coating filler to enhance corrosion protection performance *Phys. Chem. Chem. Phys.* **21** 18179–87
[39] Nair P, Nair M, Zingaro R A and Meyers E A 1994 XRD, XPS, optical and electrical studies on the conversion of SnS thin films to SnO_2 *Thin Solid Films* **239** 85–92
[40] Seko A, Togo A, Oba F and Tanaka I 2008 Structure and stability of a homologous series of tin oxides *Phys. Rev. Lett.* **100** 045702
[41] Wang J, Li H, Meng S, Zhang L, Fu X and Chen S 2017 One-pot hydrothermal synthesis of highly efficient SnO_x/Zn_2SnO_4 composite photocatalyst for the degradation of methyl orange and gaseous benzene *Appl. Catal.* B **200** 19–30
[42] Zheng Y, Zhou T, Zhang C, Mao J, Liu H and Guo Z 2016 Boosted charge transfer in SnS/SnO_2 heterostructures: toward high rate capability for sodium-ion batteries *Angew. Chem., Int. Ed.* **55** 3408–13
[43] Suryawanshi S R, Warule S S, Patil S S, Patil K R and More M A 2014 Vapor–liquid–solid growth of one-dimensional tin sulfide (SnS) nanostructures with promising field emission behavior *ACS Appl. Mater. Interfaces* **6** 2018–25
[44] Lian Q, Zhou G, Zeng X, Wu C, Wei Y, Cui C, Wei W, Chen L and Li C 2016 Carbon coated SnS/SnO_2 heterostructures wrapping on CNFs as an improved-performance anode for Li-ion batteries: lithiation-induced structural optimization upon cycling *ACS Appl. Mater. Interfaces* **8** 30256–63
[45] Bian H, Li Z, Xiao X, Schmuki P, Lu J and Li Y Y 2018 Tunable transformation between SnS and SnO_x nanostructures via facile anodization and their photoelectrochemical and photocatalytic performance *Solar RRL* **2** 1800161
[46] Bian H, Li Z, Xiao X, Schmuki P, Lu J and Li Y Y 2019 Anodic synthesis of hierarchical SnS/SnO_x hollow nanospheres and their application for high-performance Na-ion batteries *Adv. Funct. Mater.* **29** 1901000
[47] Kwoka M, Ottaviano L, Passacantando M, Santucci S, Czempik G and Szuber J 2005 XPS study of the surface chemistry of L-CVD SnO_2 thin films after oxidation *Thin Solid Films* **490** 36–42
[48] Cheng S and Conibeer G 2011 Physical properties of very thin SnS films deposited by thermal evaporation *Thin Solid Films* **520** 837–41
[49] Chetri P, Choudhury B and Choudhury A 2014 Room temperature ferromagnetism in SnO_2 nanoparticles: an experimental and density functional study *J. Mater. Chem.* C **2** 9294–302
[50] Sharma A, Tomar M and Gupta V 2012 Room temperature trace level detection of NO_2 gas using SnO_2 modified carbon nanotubes based sensor *J. Mater. Chem.* **22** 23608–16
[51] Freundlich H 1909 *Kapillarchemie, Eine Darstellung Der Chemie Der Kolloide Und Verwandter Gebiete, Von Dr Herbert Freundlich* (Leipzig: Akademische Verlagsgesellschaft)
[52] Li M, Zhou D, Zhao J, Zheng Z, He J, Hu L, Xia Z, Tang J and Liu H 2015 Resistive gas sensors based on colloidal quantum dot (CQD) solids for hydrogen sulfide detection *Sens. Actuators* B **217** 198–201
[53] Bernal E 2014 Limit of detection and limit of quantification determination in gas chromatography *Adv. Gas Chromatogr.* **3** 57–63
[54] Sacco L, Forel S, Florea I and Cojocaru C-S 2020 Ultra-sensitive NO_2 gas sensors based on single-wall carbon nanotube field effect transistors: monitoring from ppm to ppb level *Carbon* **157** 631–9
[55] van Quang V, van Dung N, Sy Trong N, Duc Hoa N, van Duy N and van Hieu N 2014 Outstanding gas-sensing performance of graphene/SnO_2 nanowire Schottky junctions *Appl. Phys. Lett.* **105** 013107
[56] Wang X, Aroonyadet N, Zhang Y, Mecklenburg M, Fang X, Chen H, Goo E and Zhou C 2014 Aligned epitaxial SnO_2 nanowires on sapphire: growth and device applications *Nano Lett.* **14** 3014–22
[57] Wang Y, Liu D, Yin J, Shang Y, Du J, Kang Z, Wang R, Chen Y, Sun D and Jiang J 2020 An ultrafast responsive NO_2 gas sensor based on a hydrogen-bonded organic framework material *Chem. Commun.* **56** 703–6
[58] Parellada-Monreal L *et al* 2020 WO_3 processed by direct laser interference patterning for NO_2 detection *Sens. Actuators* B **305** 127226
[59] Qi P, Vermesh O, Grecu M, Javey A, Wang Q, Dai H, Peng S and Cho K J 2003 Toward large arrays of multiplex functionalized carbon nanotube sensors for highly sensitive and selective molecular detection *Nano Lett.* **3** 347–51
[60] Ou J Z, Ge W, Carey B, Daeneke T, Rotbart A, Shan W, Wang Y, Fu Z, Chrimes A F and Wlodarski W 2015 Physisorption-based charge transfer in two-dimensional SnS_2 for selective and reversible NO_2 gas sensing *ACS Nano* **9** 10313–23
[61] Koteeswara Reddy N, Devika M and Gopal E S R 2015 Review on tin (II) sulfide (SnS) material: synthesis, properties, and applications *Crit. Rev. Solid State Mater. Sci.* **40** 359–98
[62] Bhattacharya P and Pang L Y 1997 *Semiconductor Optoelectronic Devices* vol 613 (River, NJ: Prentice hall upper saddle)
[63] Roondhe B and Jha P K 2018 'Haeckelite', a new low dimensional cousin of boron nitride for biosensing with ultra-fast recovery time: a first principles investigation *J. Mater. Chem.* B **6** 6796–807
[64] Anothainart K, Burgmair M, Karthigeyan A, Zimmer M and Eisele I 2003 Light enhanced NO_2 gas sensing with tin oxide at room temperature: conductance and work function measurements *Sens. Actuators* B **93** 580–4
[65] Espid E and Taghipour F 2017 UV-LED photo-activated chemical gas sensors: a review *Crit. Rev. Solid State Mater. Sci.* **42** 416–32